THE JOURNAL OF PHYSICAL CHEMISTRY A
A JOURNAL OF THE AMERICAN CHEMICAL SOCIETY

pubs.acs.org/JPCA Article

Ultraviolet Excitation of M-O_2 (M = Phenalenone, Fluorenone, Pyridine, & Acridine) Complexes Resulting in $^1O_2$

Bradley F. Parsons,* Martin R. Hulce, John R. Ackerman, Kylie A. Reardon, Emerson S. Pappas, and Lauren E. Kettler

Cite This: *J. Phys. Chem. A* 2024, 128, 2971−2981 Read Online

ACCESS | Metrics & More | Article Recommendations | Supporting Information

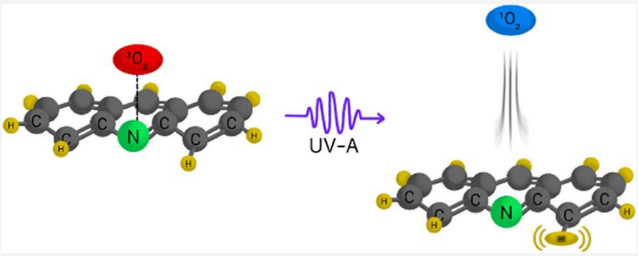

ABSTRACT: In our experiment, a trace amount of an organic molecule (M = 1*H*-phenalen-1-one, 9-fluorenone, pyridine, or acridine) was seeded into a gas mix consisting of 3% O_2 with a rare gas buffer (He or Ar) and then supersonically expanded. We excited the resulting molecular beam with ultraviolet light at either 355 nm (1*H*-phenalen-1-one, 9-fluorenone, or acridine) or 266 nm (pyridine) and used resonance enhanced multiphoton ionization (REMPI) spectroscopy to probe for the formation of O_2 in the a-$^1\Delta_g$ state, $^1O_2$. For all systems, the REMPI spectra demonstrate that ultraviolet excitation results in the formation of $^1O_2$ and the oxygen product is confirmed to be in the ground vibrational state and with an effective rotational temperature below 80 K. We then recorded the velocity map ion image of the $^1O_2$ product. From the ion images, we determined the center-of-mass translational energy distribution, $P(E_T)$, assuming photodissociation of a bimolecular M-O_2 complex. We also report results from electronic structure calculations that allow for a determination of the M-O_2 ground state binding energy. We use the complex binding energy, the energy to form $^1O_2$, and the adiabatic triplet energy for each organic molecule to determine the available energy following photodissociation. For dissociation of a bimolecular complex, this available energy may be partitioned into either center-of-mass recoil or internal degrees of freedom of the organic moiety. We use the available energy to generate a Prior distribution, which predicts statistical energy partitioning during dissociation. For low available energies, less than 0.2 eV, we find that the statistical prediction is in reasonable agreement with the experimental observations. However, at higher available energies, the experimental distribution is biased to lower center-of-mass kinetic energies compared with the statistical prediction, which suggests the complex undergoes vibrational predissociation.

I. INTRODUCTION

The ground state of molecular oxygen has two unpaired electrons, resulting in an electronic state with triplet multiplicity, the X $^3\Sigma_g^-$ state, which we designate as $^3O_2$. The lowest excited state of oxygen has all electrons paired, resulting in a singlet state, the $^1\Delta_g$ state, which we refer to as $^1O_2$. This lowest excited state lies 0.98 eV above the ground state,[1] and the lowest singlet state is observed to be cytotoxic. The latter observation has resulted in singlet oxygen being utilized for cancer treatments, where $^1O_2$ may be formed by using light to first excite a photosensitizer to a higher-lying singlet state. The excited singlet photosensitizer may undergo intersystem crossing to a triplet state, and the latter is then quenched by $^3O_2$ resulting in $^1O_2$.[2]

Direct optical excitation from the O_2 X $^3\Sigma_g^-$ state to the $^1\Delta_g$ state is disallowed. The lowest allowed electronic transition of molecular O_2 is to the B $^3\Sigma_u^-$ state, and excitation to this state accounts for the Shuman-Runge bands and continuum.[3] Moreover, while ultraviolet excitation with a 225 nm photon has sufficient energy to dissociate O_2 into O (^{3}P) products, the transition is disallowed and weak; however, previous work has demonstrated that supersonic expansion of an organic chromophore and O_2 seeded into a rare carrier gas results in enhancement of 225 nm oxygen photodissociation.[4−7] Furthermore, experiments with isoprene co-expanded with O_2 observed that ultraviolet excitation between 213 and 277 nm resulted in $^1O_2$ formation and related experiments were reviewed by Baklanov and Parker.[8,9] For these experiments, addition of the organic species into the molecular beam results in a weakly bound O_2 containing complex, M-O_2, that undergoes photodissociation leading to $^1O_2$. The M-O_2 complex has an overall triplet ground state: $^3(^1M - {}^3O_2)$ and UV excitation may result in simultaneous spin-changing transitions for both moieties that maintains the overall complex multiplicity.[9] This double spin flip (DSF) transition may be

Received: January 8, 2024
Revised: March 20, 2024
Accepted: March 20, 2024
Published: April 5, 2024

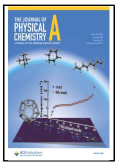

https://doi.org/10.1021/acs.jpca.4c00143

written as $^3(^1M - {}^3O_2) + h\nu \rightarrow {}^3(^3M^* - {}^1O_2)$, where ^1M and $^3M^*$ are the ground state and lowest triplet excited state of the chromophore. The minimum dissociation energy can be estimated as the sum of the adiabatic triplet state energy, the $^1O_2$ term energy, and the ground state binding energy, D_0''

$$E_{\text{threshold}} = E_{^3\text{M}} + E_{^1\text{O}_2} + D_0'' \tag{1}$$

The relationships in eq 1 are shown in Figure 1, where E_{int} is the sum of the chromophore adiabatic triplet energy and the $^1O_2$ term energy: $E_{\text{int}} = E_{^3\text{M}} + E_{^1\text{O}_2}$.

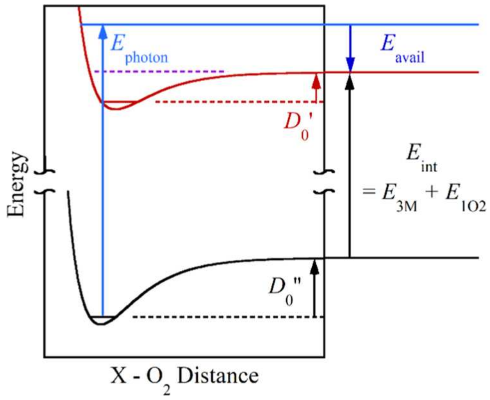

Figure 1. Schematic ground and excited state potentials along the coordinate between O_2 and the organic center-of-mass (X). The blue horizontal line and blue vertical arrow represent the photon energy, and D_0'' and D_0' are the ground and excited state complex binding energies. The internal electronic energy for both the ^3M and $^1O_2$ fragments is denoted by the vertical arrow labeled E_{int}. The purple dashed line shows the dissociation energy threshold in eq 1, which is the sum of E_{int} and D_0''.

For the excitation shown in Figure 1, the available energy, E_{avail}, is given by the photon energy, E_{photon}, minus the threshold dissociation energy from eq 1

$$E_{\text{avail}} = E_{\text{photon}} - E_{\text{threshold}} = E_{\text{photon}} - E_{^3\text{M}} - E_{^1\text{O}_2} - D_0'' \tag{2}$$

During photodissociation, the available energy from eq 2 may be partitioned into either the center-of-mass (CM) translational energy between the recoiling moieties of the complex or rotational and vibrational degrees of freedom of the moieties.

From eq 1, we expect that lowering the chromophore triplet energy will reduce the photon energy required to form $^1O_2$ through a DSF-type transition. An important motivation for the current work is to experimentally demonstrate that seeding lower triplet energy chromophores into a molecular beam indeed shifts $^1O_2$ formation into the UV-A range with photon wavelengths above 315 nm. Thus, we have selected four organic molecules with a range of triplet energies. These chromophores include the aza-aromatic molecules pyridine and acridine with adiabatic triplet energies of 3.44 and 1.96 eV, respectively.[10,11] We have also included the aromatic carbonyls fluorenone and 1*H*-phenalen-1-one and the latter we refer to as phenalenone. The fluorenone adiabatic triplet energy was measured to be 2.31 eV using photoelectron spectroscopy,[12] and phosphorescence spectra gave the lowest adiabatic triplet state of phenalenone to be 1.91 eV.[13] The structures of these molecules are summarized in Figure 2.

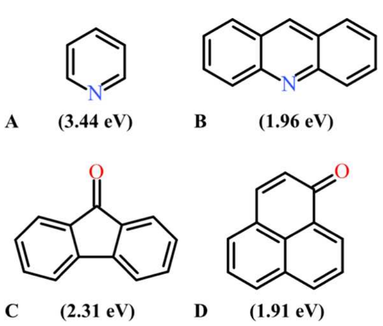

Figure 2. Structures of the molecules from this study. (A) pyridine, (B) acridine, (C) fluorenone, and (D) phenalenone. The number in parentheses below each molecule is the adiabatic triplet energy taken from refs 10−13.

The range of adiabatic triplet energies for these molecules allows for our experiments to probe the reduced $^1O_2$ threshold energy from eq 1. Moreover, our experiments sample a range of available energies from eq 2, which allows us to explore energy partitioning during photodissociation. How energy is partitioned between CM translation and rotational and vibrational motions of the chromophore is indicative of the photodissociation mechanism. In our previous work, photodissociation was analyzed in terms of a statistical mechanism;[14,15] however, the current work gives evidence for photodissociation via vibrational predissociation.

In the next section, we discuss both the computational and experimental methods used for our work. In Section III, we first present computational results for the complex binding energy and adiabatic and vertical triplet energies for the chromophores. We then report results of REMPI and velocity map ion imaging, VMI, experiments to demonstrate the formation of $^1O_2$ and measure the CM recoil kinetic energy distribution assuming dissociation of a bimolecular complex. In Section IV, we evaluate the experimental data to assess the likely dissociation mechanism for the complex, and in Section V, we present a brief conclusion.

II. METHODS

All electronic structure calculations are carried out using the ORCA program suite.[16] For the pyridine-O_2 complex, geometry optimization is performed using four density functional theory (DFT) methods: PBE, M06, BLYP, and B3LYP.[17−21] For acridine, fluorenone, and phenalenone complexes, calculations are performed using only the PBE and M06 methods. For all systems, we use the aug-cc-pV*n*Z basis sets (n = D, T, Q).[22] For the bimolecular complexes, we include dispersion corrections for the PBE, BLYP, and B3LYP calculations using the D3BJ method in ORCA while for M06 we use the D3-Zero method.[23] When calculating the M-O_2 binding energy our results are corrected for basis set superposition error (BSSE) using a counterpoise correction.[24] For all complexes, the frequency analysis and single point energy calculations were performed using the same DFT method and basis set as was used for the initial geometry optimization.

Using the ORCA program suite, the relative energies for the singlet and triplet states for all four organic molecules are determined using the PBE and M06 DFT methods with the aug-cc-pV*n*Z basis sets (n = T, Q). We use these methods to optimize the structure for either the singlet or the triplet state. We then determined the harmonic vibrational frequencies and single point energies. For all molecules, the frequency analysis and single point energies were calculated using the same DFT method and basis set as was used for the initial geometry optimization. We then determine the adiabatic and vertical triplet excitation energy relative to the ground state, and the latter energy is corrected for the zero-point vibrational energy of both states.

For these experiments, 1*H*-phenalen-1-one (phenalenone) is first synthesized using a Friedel−Crafts procedure[25] modified to facilitate the workup and chromatographic purification. For the synthesis, a 100 mL round-bottom flask is equipped with a stirring bar, Claisen adapter, 10 mL constant pressure addition funnel, condenser, and drying tube that is charged with anhydrous aluminum trichloride (4.00 g, 30.0 mmol) and methylene chloride (10 mL). Stirring is begun and the flask is cooled to 0 °C using an ice−water bath. (*E*)-Cinnamoyl chloride[26] (1.67 g, 10.0 mmol) in methylene chloride (10 mL) is added dropwise, followed by dropwise addition of a solution of naphthalene (1.28 g, 10.0 mmol) in methylene chloride (10 mL). Once these additions are complete, the ice−water bath is removed and the flask is heated at reflux for 3 h. After this time, the reaction is cooled to room temperature and then poured into rapidly stirring, ice-cold 2 M hydrochloric acid (30 mL). The reaction flask is rinsed well with methylene chloride (3 × 10 mL), and the rinsings are added to the stirring HCl solution.

The resulting mixture is vacuum-filtered, the collected solids are stirred with methylene chloride (50 mL), and the resulting suspension is also vacuum-filtered. The filtrates are combined and transferred to a separatory funnel. The methylene chloride extract is removed, and the aqueous phase was washed with methylene chloride (30 mL). The methylene chloride extracts are combined, dried with anhydrous sodium sulfate, filtered, and concentrated by rotary evaporation to give 1.61 g of a dark orange solid. This solid is purified by flash column chromatography (3:1 hexanes:ethyl acetate) to give 1.13 g (63%) of yellow, crystalline 1*H*-phenalen-1-one. TLC rf 0.57 (3:1 hexanes:ethyl acetate); 0.35 (CH_2Cl_2). Mp 151−154 °C; lit mp 153.5−154 °C.[27] Figure S1 in the Supporting Information gives the infrared (ATR) spectrum with the following observed bands: IR 3040 (w), 1638 (s), 1619 (s), 1587 (s), 1576 (s), 829 (m), 773 (m) cm^{-1}. Figures S2 and S3 in the Supporting Information give the ^{1}H and ^{13}C NMR spectra of phenalenone with the following chemical shifts: ^{1}H NMR ($CDCl_3$) δ 8.63 (dd, J = 7.4, 1.2 Hz, 1H), 8.21 (dd, J = 8.1, 1.1 Hz, 1H), 8.03 (dd, J = 8.2, 0.9 Hz, 1H), 7.83−7.71 (m, 3H), 7.59 (dd, J = 8.2, 7.0 Hz, 1H), 6.74 (d, J = 9.8 Hz, 1H) ppm. ^{13}C NMR ($CDCl_3$) δ: 185.7, 141.8, 134.9, 132.2, 131.9, 131.4, 130.4, 129.5, 129.3, 127.9, 127.6, 127.1, 126.6 ppm. Finally, Figure S4 in the Supporting Information shows the EI mass spectrum of the phenalenone product m/z 180 ($M^{+\cdot}$, 79), 152 (100).

For our other experiments, samples of pyridine (Thermo-Scientific, 99.5+% Ultrapure Spectrophotometric grade), acridine (Thermo Scientific, 97%), and fluorenone (TCI, >98.0%) are used as received. We introduce these organic molecules into the gas phase using an Even-Lavie nozzle (Lamid, 150 mm orifice, ~20 μs pulse).[28,29] For our experiments, about 10 mg of the sample is placed inside a sample holder using a glass wool immobilizer. For pyridine, the nozzle is unheated and we expand with a carrier gas mix consisting of 3% O_2 in a He buffer. For phenalenone, fluorenone, and acridine, the nozzle is heated about 10 °C above the melting point, and we use a carrier gas consisting of 3% O_2 in an Ar buffer. For all experiments, the nozzle stagnation pressure is 200 psig (15 bar) and the supersonic expansion is skimmed 100 mm downstream from the nozzle using a 3 mm skimmer (Beam Dynamics). The resulting molecular beam travels along the cylindrical axis of a four-plate ion optics stack, which we use for conventional velocity map ion imaging.[30] Between the first (repeller) and second (extractor) ion optics, we cross the molecular beam with photons at either 266 or 355 nm from an Nd:YAG laser (Amplitude SureLite EX, 6 ns pulse). This laser photodissociates weakly bound complexes in the molecular beam yielding O_2 fragments. We then resonantly ionize any O_2 a $^1\Delta_g$ products with photons near 312 nm from the frequency doubled output of a Nd:YAG pumped dye laser (Spectra Physics Lab-190−10 Hz, 10 ns pulse & Sirah Cobra Stretch).[31,32]

For all experiments, the photolysis laser is telescoped to a 3 mm beam diameter and completely overlaps the probe laser, and the latter is focused using a 200 mm lens giving an estimated beam diameter of 20 μm. For both lasers, we use a polarizing beam splitter (ThorLabs) and tunable waveplate (Alphalas GmbH) to control input laser power during experiments. The relative timing between the lasers and the pulsed nozzle is controlled using three digital delay generators (SRS DG535 and Quantum Composers 9514+).

Following resonant ionization, O_2^+ is projected onto a 2D position-sensitive detector, and the velocity map ion image is recorded using a CCD camera (QCam Fast 1394). The VMI ion optics magnify the resulting image such that the observed velocity, v_{obs}, is larger than the actual velocity, v_{actual}, leading to a magnification factor given by $M = v_{obs}/v_{actual}$. We calibrate the experimental magnification factor using photodissociation of methyl iodide at 266 nm followed by resonant ionization of the resulting I ($^2P_{3/2}$) and I* ($^2P_{1/2}$) products.[33]

We record the 2 + 1 REMPI spectrum for $^1O_2$ by scanning the dye laser wavelength while measuring the detector signal for $m/z = 32$.[14] To avoid detector saturation, we select the ion optics voltage to spatially focus the O_2^+ and use a boxcar integrator (SRS SR250) to bin the total $m/z = 32$ signal. The resulting averaged signal is then recorded using a USB data acquisition device (LabJack U3−HV).

III. RESULTS

To determine the available energy using eq 1, we need the ground state complex binding energy, D_0''. We have previously determined such binding energies using *ab initio* MP2 electronic structure calculations.[14,15,34] Our previous MP2/aug-cc-pVDZ calculations for pyridine-O_2 found the most stable geometry with the O_2 moiety above the ring with the complex having approximate C_s symmetry and a BSSE-corrected binding energy of 456 cm^{-1} (0.056 eV);[34] however, MP2 calculations with large basis sets may become cost prohibitive for complexes including larger organic molecules. Therefore, we performed a series of calculations for the pyridine-O_2 complex to evaluate four DFT methods: BLYP, B3LYP, PBE, and M06 with the goal of determining which methods provide binding energies consistent with MP2 results. For each method, the geometry was first optimized starting from a C_s complex geometry with O_2 above the plane of the ring using the aug-cc-pVnZ (n = D, T, Q) basis sets. Figure S5 in the Supporting Information provides the approximate structure for the optimized pyridine-O_2 complex, and Table

S1 in the Supporting Information gives the optimized Cartesian coordinates from our PBE/aug-cc-pVQZ calculation. For all methods, the energies were corrected for both BSSE and dispersion interactions, as discussed in Section II. Figure 3 presents the pyridine-O_2 binding energy from the DFT calculations as a function of the basis set Cardinal number, *n*. As shown in Figure 3, both the BLYP and B3LYP methods give unsatisfactory results with binding energies that are consistently smaller (less negative) than the MP2/aug-cc-pVDZ calculated energy, which is shown as the dashed green line in the figure. However, as shown in Figure 3 and reported in Table 1, both the PBE and M06 methods give more satisfactory results with binding energies of 382 and 349 cm^{-1}, respectively, for the largest basis set: aug-cc-pVQZ.

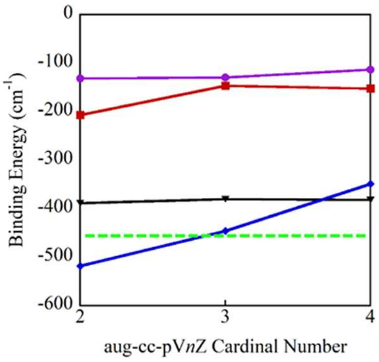

Figure 3. BSSE-corrected pyridine-O_2 binding energy as a function of the aug-cc-pV*n*Z basis set Cardinal number, *n* from DFT calculations. The purple line is the result from the BLYP method, the red line is from the B3LYP method, the black line is for the PBE method, and the blue line is from our M06 calculations. Finally, the dashed green line corresponds to the energy obtained from our previous MP2/aug-cc-pVDZ calculations.

Table 1. Complex Binding Energies in Units of cm^{-1}

method	phenalenone-O_2	fluorenone-O_2	acridine-O_2	pyridine-O_2
PBE/aug-cc-pVDZ//D3	549	516	523	388
PBE/aug-cc-pVTZ//D3	510	485	513	380
PBE/aug-cc-pVQZ//D3	506	479	514	382
M06/aug-cc-pVDZ//D3	969	755	762	518
M06/aug-cc-pVTZ//D3	676	624	555	445
M06/aug-cc-pVQZ//D3	604	550	480	349

For the phenalenone, fluorenone, and acridine-O_2 complexes, we performed calculations using only the PBE and M06 methods with aug-cc-pV*n*Z (*n* = D, T, or Q) basis sets. For the geometry optimization, both fluorenone and acridine complexes were started from initial C_s symmetry structures; however, this was not possible for phenalenone-O_2 due to the lack of a symmetry plane. For the latter, the O_2 moiety was started above the center of the organic ring system and parallel with the plane of the ring. Figures S6−S8 in the Supporting Information show the approximate structure of the individual complexes, and Tables S2−S4 in the Supporting Information give the optimized Cartesian coordinates from our PBE/aug-cc-pVQZ calculations. For the phenalenone-O_2 complex, the binding energy is found to be 506 cm^{-1} (0.063 eV) from the PBE/aug-cc-pVQZ calculation or 604 cm^{-1} (0.075 eV) from the M06/aug-cc-pVQZ calculation. The calculations show the fluorenone-O_2 complex to be more weakly bound with binding energies of 479 cm^{-1} (0.059 eV) from the PBE/aug-cc-pVQZ and 550 cm^{-1} (0.068 eV) from the M06/aug-cc-pVQZ. The acridine-O_2 complex has binding energies of 514 cm^{-1} (0.064 eV) and 480 cm^{-1} (0.060 eV) from the PBE and M06 calculations, respectively. Finally, we note that while our previous calculations with pyridine, quinoline, and β-ionone found several structures for the bimolecular complex with O_2, here we sought to locate only strongly bound structures. While other weakly bound structures may be present in the molecular beam, any structure with a lower binding energy would have a larger available energy and could thus partition more energy into CM translation.

For all four organic chromophores, we have also calculated the adiabatic (minimum) and vertical triplet state energies relative to the singlet ground state. For these calculations, we used the PBE and M06 DFT methods with the aug-cc-pV*n*Z (*n* = T, Q) basis sets. The adiabatic triplet energies were corrected for the zero-point vibrational energy of the singlet ground and triplet excited states using the unscaled harmonic vibrational frequencies, obtained at the same level of theory as the geometry optimization. We have reported the resulting harmonic vibrational frequencies from our PBE/aug-cc-pVQZ optimized geometries in Tables S5−S12 in the Supporting Information. In Table 2, we report the resulting adiabatic and vertical triplet energies from our PBE/aug-cc-pVQZ calculations as well as the lowest experimental triplet energy for all four organic molecules. We note that the calculated adiabatic triplet energy is consistently less than the experimental value, and the average difference between the calculation and experiment is −0.15 eV. Furthermore, the vertical triplet energy is higher than the adiabatic, as is expected since the ground and triplet excited state minimum geometries are not the same. Consequently, for all four organic molecules, we expect that vertical excitation from the singlet ground state to the triplet excited state should result in some vibrational excitation. Finally, Tables S13 and S14 in the Supporting Information give the adiabatic and vertical triplet energies from all PBE and M06 calculations performed for this study.

Table 2. Adiabatic and Vertical Excitation Energies from PBE/aug-cc-pVQZ Calculated Geometries[a]

	$E(T_1)_{ad,exp}$	$E(T_1)_{ad,calc}$	$E(T_1)_{vert,calc}$
phenalenone	1.91[b]	1.68	2.41
fluorenone	2.31[c]	2.20	2.36
pyridine	3.44[d]	3.38	4.06
acridine	1.96[e]	1.75	2.08

[a] All energies are reported in eV. [b] Reference13. [c] Reference12. [d] Reference11. [e] Reference10.

We use eq 1 to find the minimum energy for $^1O_2$ formation from the complex binding energy, given in Table 1, the experimental adiabatic triplet energy, given in Table 2, and the $^1O_2$ term energy of 0.98 eV.[1] We determined the threshold energy using the complex binding energy from both the PBE/aug-cc-pVQZ and the M06/aug-cc-pVQZ calculations, and the results are reported in Table 3 along with the wavelengths for an Nd:YAG laser harmonic with photon energy above the

Table 3. DSF Threshold Energy for $^1O_2$ Formation Calculated Using the PBE/aug-cc-pVQZ or M06/aug-cc-pVQZ Complex Binding Energy[a]

	$E_{\text{threshold}}$[a]	$\lambda_{\text{excitation}}$ (nm)	E_{photon}	E_{avail}[a]
phenalenone	2.95 (2.97)	355	3.49	0.54 (0.52)
fluorenone	3.35 (3.36)	355	3.49	0.14 (0.13)
pyridine	4.47 (4.46)	266	4.66	0.19 (0.20)
acridine	3.00 (3.00)	355	3.49	0.49 (0.49)

[a] All energies are given in eV. M06 numbers given in parentheses.

energy threshold. In Table 3, we also report E_{avail} using eq 2 calculated assuming excitation at the given wavelength.

We next experimentally verify $^1O_2$ formation by seeding each organic molecule in a gas mix consisting of 3% O_2 in an inert carrier and supersonically expanding the gas mix. We note these nozzle conditions are similar to those in previous experiments from our lab where we reported rotational temperatures as low as 5 K,[35] and under such low-temperature conditions, we expect the formation of organic-O_2 (M-O_2) complexes. We then excite the resulting molecular beam using the wavelengths given in Table 3 and probe for $^1O_2$ by recording the resonance enhanced multiphoton ionization (REMPI) spectrum using the d $^1\Pi_g$ (v' = 3) ←← a$^1\Delta_g$ (v'' = 0) transition accessible near 312 nm.[31,32]

Figure 4 shows the resulting $^1O_2$ REMPI spectrum from co-expansion of phenalenone. The spectra in Figure 4 were recorded at a nozzle temperature between 160 and 170 °C, which is above the melting point of 154 °C.[27] The $^1O_2$ signal was observed to increase with backing pressure as would be expected for complex formation from O_2 gas and phenalenone vapor with the latter in equilibrium with the liquid. We attempted to assess the temperature dependence of the $^1O_2$ signal; however, the peak nozzle timing drifts with increasing temperature, and this drift prevented quantitative measurements.

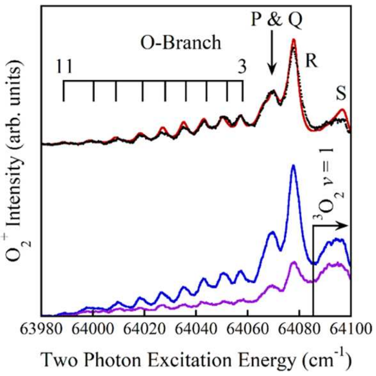

Figure 4. The blue curve is the raw observed m/z = 32 (O_2^+) ion signal from 355 nm photodissociation of phenalenone-O_2 with resonant ionization at 312 nm, and the purple curve corresponds to the weak $^1O_2$ background signal with the 355 nm laser arriving 100 ns after the probe laser. The black points at the top are the difference between the blue and purple curves (background subtraction), and the red curve is a simulated $^1O_2$ REMPI spectrum assuming an 80 K rotational Boltzmann distribution. In the raw spectra, blue and purple curves, much of the signal in the broad band above 64085 cm^{-1} results from a background due to vibrationally excited (v = 1) $^3O_2$ formed by the high nozzle temperature, and this region is indicated by the horizontal arrow in the lower frame.

The blue curve in Figure 4 shows the experimental data with the 355 nm photodissociation laser arriving 100 ns *before* the 312 nm probe laser, while the purple curve was recorded with the photolysis laser timed 100 ns *after* the probe laser. We have subtracted the purple (probe-only) spectrum from the blue (photolysis + probe) spectrum to obtain the $^1O_2$ REMPI spectrum due to 355 nm photolysis, which are the black points in Figure 4 (top). The red curve in Figure 4 is a simulation for the d $^1\Pi_g$ (v' = 3) ←← a$^1\Delta_g$ (v'' = 0) transition using the PGopher program with a rotational temperature of 80 K.[36] Figures S9−S11 in the Supporting Information show the corresponding spectra from photolysis following introduction of fluorenone, pyridine, or acridine into the molecular beam.

The simulation (red) in Figure 4 reasonably reproduces the 355 nm spectrum (black points), which demonstrates the formation of $^1O_2$ during the experiment. We also performed control experiments by expanding either the O_2/Ar or the O_2/He with no organic chromophore seeded into the molecular beam. For the control experiments, we observed no resonant O_2^+ signal at a nozzle temperature below about 150 °C. At nozzle temperatures above 150 °C, we did observe a O_2^+ background signal that results in the broad shoulder at two photon energies above 64085 cm^{-1}, which is indicated by the horizontal arrow in the lower frame of Figure 4. The high-temperature background, which contributes to the raw experimental spectra only above 64085 cm^{-1}, overlaps the S-Branch in Figure 4 and corresponds to the two-photon allowed transition originating from vibrationally excited ground state $^3O_2$:$^3\Pi_g$ (v' = 0) ←← $X^3\Sigma_g^-$ (v'' = 1).[31] As such, this high-temperature background is due to the increased population of vibrationally excited $^3O_2$ at higher nozzle temperatures but does not correspond to the formation of $^1O_2$. As no $^1O_2$ spectral signature was observed without the organic chromophore seeded into the molecular beam along with the previously discussed pressure and temperature dependence, we conclude that the $^1O_2$ spectrum in Figure 4 results from a complex between phenalenone and O_2.

We note that from the simulation (red) in Figure 4, $^1O_2$ is produced with an effective rotational temperature of 80 K. Figures S9 and S11 in the Supporting Information show the $^1O_2$ REMPI spectra following introduction of fluorenone or acridine into the molecular beam and subsequent photolysis at 355 nm resulting in $^1O_2$ (v = 0). From the simulation of the spectra, the effective $^1O_2$ rotational temperature was 55 or 60 K, respectively. Figure S10 in the Supporting Information presents the $^1O_2$ REMPI spectrum from the introduction of pyridine with 266 nm photolysis and with an effective rotational temperature of 75 K. Thus, for all experiments, $^1O_2$ is formed with a rotational temperature at or below 80 K, which is consistent with our previous observations.[14,15]

After confirming $^1O_2$ formation, we fixed the ionization laser to the maximum band from the $^1O_2$ REMPI spectrum, which corresponds to the lowest rotational levels probed through R-branch-type transitions. We then recorded sets of ion images, with the photolysis laser timed either: (1) 100 ns *before* the ionization laser (photolysis + probe images) or (2) 100 ns *after* the ionization laser (probe-only images). The probe-only images showed very slow $^1O_2$ with a maximum intensity at the image center corresponding to the location of the molecular beam spot. We then subtract the probe-only images from the photolysis + probe images, and the resulting subtracted ion image for phenalenone-O_2 appears as the inset in Figure 5 where the vertical arrow indicates the polarization direction for both photolysis and probe lasers.

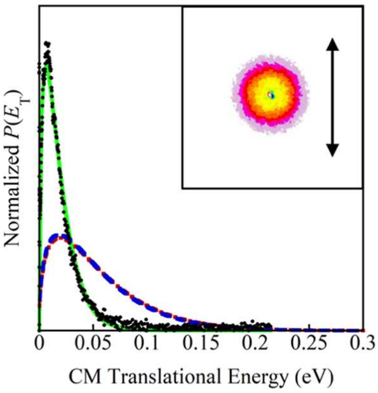

Figure 5. The inset gives the O_2^+ ion image with phenalenone seeded into the molecular beam and at a 3.49 eV (355 nm) photolysis photon energy. The vertical arrow in the ion image shows the polarization direction for the photolysis and probe lasers. In the image, the intensity of the O_2^+ signal is a maximum at the center (blue/green/yellow) and decreases moving to the edge (red/light purple). The black points correspond to the experimental $P(E_T)$ assuming dissociation of bimolecular $C_{13}H_8O{-}O_2$ and the green curve corresponds to a Boltzmann fit to the data with a temperature of 144 K. The red curve gives the statistical Prior distribution using the binding energy from the PBE/aug-cc-pVQZ//D3 calculation and the unscaled PBE/aug-cc-pVQZ frequencies for triplet phenalenone. The blue curve shows the statistical distribution with the binding energy from our M06/aug-cc-pVQZ//D3 calculations and the unscaled M06/aug-cc-pVQZ frequencies of triplet phenalenone.

We then determined the $^1O_2$ ($v = 0$) velocity distribution, $P(v)$, from the ion image in Figure 5 by transforming the image using the Basex program.[37] We converted the O_2 velocity distribution into a CM translational energy distribution, $P(E_T)$, with the CM translational energy given by $E_T = \left(\frac{m_A + m_B}{m_B}\right)\frac{1}{2}m_A v_A^2$, where m_A and v_A are the mass and velocity of the detected fragment, respectively, and m_B is the mass of the undetected fragment. To determine the CM translational energy, we must know the mass of the undetected partner fragment. Since no $^1O_2$ was observed without an organic chromophore seeded into the molecular beam, we conclude the signal originates from a cluster of the form $(C_{13}H_8O)_n$-O_2 with $n \geq 1$ and the unobserved partner fragment in Figure 5 must contain phenalenone. For previous experiments with quinoline-O_2, we recorded a mass spectrum of the molecular beam using the focused 312 nm laser for ionization and observed a weak signal for the bimolecular complex with no signal observed for higher-order clusters.[15] For quinoline, 312 nm photons are nearly resonant with the S_2 ($\pi\pi^*$) excited state,[38] which may enhance the ionization of quinoline-containing clusters. We attempted similar experiments for the species in this study; however, no discernible signal was observed in the mass spectrum for either a bimolecular or a higher-order cluster.

Without the mass spectrum, we cannot definitively state the molecular beam does not contain higher-order complexes; however, we note for dissociation from a higher-order cluster the partner mass, m_B, would be larger and so the kinematic mass term, $\left(\frac{m_A + m_B}{m_B}\right)$, would be closer to unity. As a result, for a given $^1O_2$ velocity, the calculated CM recoil kinetic energy would be smaller for dissociation from higher-order clusters and this would result in a more narrow kinetic energy distribution for a given O_2 velocity distribution. For our analysis, we assume dissociation from a bimolecular complex, but we note that the resulting $P(E_T)$ is expected to be narrower if higher-order clusters significantly contribute to the observed signal. For phenalenone-O_2, the resulting $P(E_T)$ value is shown in Figure 5.

The melting point of fluorenone is 84 °C,[39] and at a nozzle temperature of about 90 °C, we observed $^1O_2$ due to photolysis at 355 nm, Figure S9. In Figure 6, we present the CM recoil kinetic energy distribution for fluorenone-O_2, which was obtained from the subtracted ion image shown in the inset. Liquid pyridine was seeded into the molecular beam using an unheated nozzle, and we observed $^1O_2$ following photolysis at 266 nm, as shown in Figure S10. Figure 7 presents the CM recoil kinetic energy distribution along with the subtracted ion image. Finally, the melting point of acridine is 110 °C,[40] and at a nozzle temperature between 115 and 120 °C, we observed an onset in the $^1O_2$ signal for photolysis at 355 nm, Figure S11. Figure 8 presents the CM $P(E_T)$ and subtracted ion image from the introduction of acridine into the molecular beam.

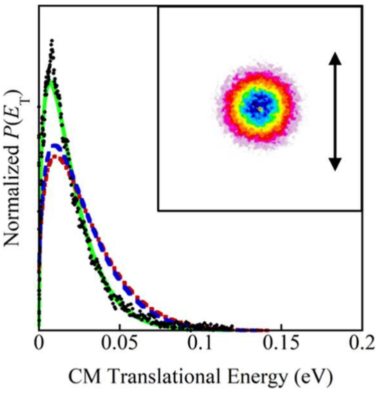

Figure 6. The inset ion image is from $^1O_2$ formed with fluorenone seeded into the molecular beam at a 3.49 eV (355 nm) photolysis photon energy. The black arrow gives the polarization direction for both photolysis and probe lasers, and the black points are the experimental $P(E_T)$ assuming dissociation of bimolecular $C_{13}H_8O{-}O_2$ at 3.49 eV (355 nm). The green curve is a fit to a Boltzmann distribution with a resulting temperature of 156 K. The red curve gives the statistical Prior distribution using the binding energy from the PBE/aug-cc-pVQZ//D3 calculation and the unscaled PBE/aug-cc-pVQZ frequencies for triplet fluorenone. The blue curve shows the statistical distribution with the binding energy from our M06/aug-cc-pVQZ//D3 calculations and the unscaled M06/aug-cc-pVQZ frequencies of triplet fluorenone.

In Figures 5−8, we also show in green the results of a Boltzmann fit to the experimental CM $P(E_T)$. The resulting translational temperatures were 144 K for either phenalenone-O_2 or acridine-O_2, 156 K for fluorenone-O_2, and 281 K for pyridine-O_2. In these figures, we have also presented the predicted $P(E_T)$ for a statistical partitioning of available energy into the fragments during photodissociation. Since all ion images were recorded by resonantly ionizing $^1O_2$ from the lowest rotational levels of the ground vibrational state, the oxygen fragment internal energy is simply the term energy, 0.98 eV. Thus, for all systems, the available energy given in Table 3 may be partitioned only into either CM translation or

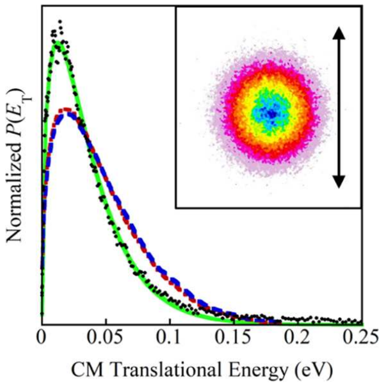

Figure 7. The inset ion image is from $^1O_2$ formed with pyridine seeded into the molecular beam at a 4.66 eV (266 nm) photolysis photon energy. The black arrow gives the polarization direction for both photolysis and probe lasers, and the black points are the experimental $P(E_T)$ assuming dissociation of bimolecular $C_5H_5N{-}O_2$. The green curve corresponds to a Boltzmann fit to the data with a resulting temperature of 281 K. The red curve gives the statistical Prior distribution using the binding energy from the PBE/aug-cc-pVQZ//D3 calculation and the unscaled PBE/aug-cc-pVQZ frequencies for triplet pyridine. The blue curve shows the statistical distribution with the binding energy from our M06/aug-cc-pVQZ//D3 calculations and the unscaled M06/aug-cc-pVQZ frequencies of triplet pyridine.

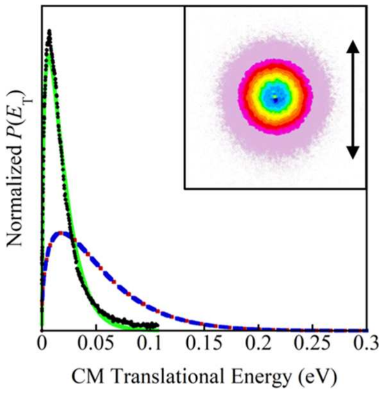

Figure 8. The inset ion image is from $^1O_2$ formed with acridine seeded into the molecular beam at a 3.49 eV (355 nm) photolysis photon energy. The black arrow gives the polarization direction for both photolysis and probe lasers, and the black points are the experimental $P(E_T)$ assuming dissociation of bimolecular $C_{13}H_9N{-}O_2$. The green curve corresponds to a Boltzmann fit to the data with a resulting temperature of 144 K. The red curve gives the statistical Prior distribution using the binding energy from the PBE/aug-cc-pVQZ//D3 calculation and the unscaled PBE/aug-cc-pVQZ frequencies for triplet acridine. The blue curve shows the statistical distribution with the binding energy from our M06/aug-cc-pVQZ//D3 calculations and the unscaled M06/aug-cc-pVQZ frequencies of triplet acridine.

rotational or vibrational degrees of freedom of the organic fragment. We model the statistical $P(E_T)$ as a Prior distribution using the rotational constants and the vibrational frequencies of the triplet organic fragment, which are taken from our electronic structure calculations. The resulting distributions are given as the curves in Figures 5 and 8. In these figures, the red curve is the result of using the available energy and unscaled harmonic vibrational frequencies from the PBE/aug-cc-pVQZ calculations while the blue curve uses the frequencies and energies from the M06/aug-cc-pVQZ calculations.

From the normalized experimental CM translational energy distribution and from the normalized Prior distributions, we also determined the average CM kinetic energy as $E_{T,ave} = \int E_T P(E_T) dE_T$. These averaged values are given in Table 4.

Table 4. Average CM Translational Energy from the Experimental and Statistical Distributions Given in Figures 5 and 8[a]

	$E_{T,ave,exp}$	$E_{T,ave,Prior}$	PSV (%)
fluorenone	0.025	0.028 (0.026)	93.1 (94.9)
pyridine	0.046	0.047 (0.049)	98.8 (97.6)
acridine	0.020	0.052 (0.052)	59.4 (59.3)
phenalenone	0.027	0.055 (0.053)	61.2 (62.7)

[a] The averaged energies from the Prior distribution and phase space volume are given for both the PBE/aug-cc-pVQZ and M06/aug-cc-pVQZ distributions with the latter given in parentheses. All reported energies are in eV.

Alternatively, we can also more quantitatively compare the experimental and Prior distributions by calculating the entropy deficiency, *DS*, which is given in eq 3:[41]

$$\mathrm{DS}(E_{\text{avail}}) = S_{\text{Prior}}(E_{\text{avail}}) - S_{\text{exp}}(E_{\text{avail}}) = \int_0^{E_{\text{avail}}} P_{T,\text{exp}}(\varepsilon) \ln\left[\frac{P_{\text{T,exp}}(\varepsilon)}{P_{\text{T,Prior}}(\varepsilon)}\right] d\varepsilon \quad (3)$$

where $P_{\text{T,exp}}(\varepsilon)$ and $P_{\text{T,Prior}}(\varepsilon)$ are the experimental and Prior distributions, respectively. Since the statistical distribution is a maximum entropy distribution, then DS is a non-negative number. From the resulting entropy deficiency, we then determine the effective volume of phase space, PSV, sampled by fragments during dissociation as PSV = $e^{-\mathrm{DS}}$. In Table 4, we report PSV values for all systems considered here.

Finally, we note that the Prior distributions in Figures 5−8, and the values given in Table 4 are quite similar using either the PBE or M06 calculations. Since the complex binding energy, D_0'', is the smallest contribution to the available energy using eq 2, the resulting energies given in Table 3 are nearly identical for either the PBE or M06 calculations. Moreover, the average difference between the PBE and M06 harmonic vibrational frequencies for the lowest triplet state of these organic molecules was found to be 13 cm^{-1}. Therefore, the similar binding energies and harmonic frequencies result in similar energy partitioning for the Prior distributions using either DFT method.

IV. DISCUSSION

At nozzle temperatures above about 150 °C, we observed a background due to resonant ionization of vibrationally excited $^3O_2$, and this background appears above 64085 cm^{-1} in the REMPI spectra shown in Figure 4. However, for all experiments, there is a $^1O_2$ background that results due to the 312 nm probe laser, shown as the purple trace in Figure 4 and Figures S9−S11. To drive the two-photon transition, the 312 nm probe laser, with an original beam diameter of about 5 mm, was focused by using an f = 200 mm lens. For a Gaussian beam, the resulting focused diameter would be about 20 μm. For our experiments, the probe laser was adjusted to minimize the background signal and typically delivered between 1 and 2 mJ/pulse with a 10 ns pulse width, which corresponds to between 3 and 6 × 10^{14} W/m^2. For all experiments, the photolysis laser had a telescoped beam diameter of about 3 mm and completely overlapped the focused probe laser. The photolysis laser typically delivered about 2 mJ/pulse with a 6 ns pulse width, which corresponds to about 5 × 10^{10} W/m^2.

Our experiments indicated that both the 312 nm background signal due to $^1O_2$, purple curve in Figure 4 and the 266 or 355 nm photolysis signals varied linearly with laser power, consistent with a one photon transition assuming the resonant step is saturated. Under normal experimental conditions, the $^1O_2$ background signal, purple curve, is less than 1/3 of the intensity due to the photolysis signal despite the significantly higher power per unit area for the probe laser. This indicates that the $^1O_2$ background signal originates from a process having a combination of either (1) a significantly weaker absorption cross section or (2) a species having a lower number density in the molecular beam. Ion images of the $^1O_2$ background signal resemble a molecular beam spot, indicating very slow fragments from photodissociation. The latter would be consistent with photodissociation from higher-order clusters of the form M_n-O_2, which we expect to have a lower number density in the molecular beam. Thus, we tentatively attribute the weak $^1O_2$ background to photodissociation of higher-order clusters, although conclusive evidence would require a mass spectrum of the molecular beam using 118 nm (10.5 eV) light for soft ionization.

We next consider the experimental $P(E_T)$ and Prior distributions shown in Figures 5−8. For fluorenone-O_2, the average experimental CM translational energy, given in Table 4, was 0.025 eV, which is comparable to the average values from the Prior distributions. Moreover, calculation of the entropy deficiency between the Prior and experimental distributions indicates that 93−95% of the phase space volume is sampled during cluster dissociation, Table 4. Likewise, for pyridine-O_2, the average experimental CM translational energy was comparable with the corresponding values from the Prior distributions, and over 98% of the phase space is sampled during dissociation. From Table 3, the available energy for photodissociation of the fluorenone-O_2 complex was calculated as 0.13−0.14 eV, while for pyridine-O_2, the available energy was calculated to be between 0.19 and 0.20 eV. Alternatively, for phenalenone-O_2, the calculated available energy, Table 3, was significantly higher at between 0.52 and 0.54 eV; however, the average experimental CM translational energy was significantly lower compared with the statistical predictions, Table 4. Moreover, less than 63% of the phase space is sampled during dissociation of phenalenone-O_2. Finally, for acridine-O_2, the available energy was calculated as 0.49 eV, Table 3, but the average experimental CM translational energy was again lower than the statistical prediction and less than 60% of phase space was sampled during dissociation, Table 4.

We now consider the discrepancy between the experimental and statistical $P(E_T)$, observed particularly for phenalenone-O_2 and acridine-O_2, Figures 5 and 8. We first compare these observations with our previous work for the quinoline-O_2 and β-ionone-O_2 complexes, which were photodissociated at 312 nm (3.97 eV).[14,15] For quinoline, the adiabatic triplet energy was reported as 2.79 eV, and for quinoline-O_2, the available energy was 0.11 eV and the experimental and statistical $P(E_T)$ showed good agreement.[15,42] For β-ionone, the lowest triplet energy was measured from solution phase experiments to be 2.38 eV.[43−45] Our previous electronic structure calculations gave the adiabatic triplet energy of 2.04 eV and the β-ionone-O_2 complex binding energy was calculated as 0.08 eV.[14] For β-ionone-O_2 photodissociation at 312 nm, the available energy is then in the range of 0.53−0.87 eV and our observed experimental $P(E_T)$ was somewhat colder than statistical.[14] Thus, for low available energies, the experimental $P(E_T)$ appears close to statistical as exhibited by quinoline (0.11 eV),[15] fluorenone (0.13−0.14 eV), and pyridine (0.19−0.20 eV) where the number in parentheses is the available energy. Alternatively, for higher available energies, the experimental $P(E_T)$ appears to be colder than statistical as observed with β-ionone (0.53−0.87 eV),[14] acridine (0.49 eV), and phenalenone (0.52−0.54 eV).

During our experiment, the organic chromophore is entrained in a molecular beam using a supersonic expansion. While our current experiments used a heated Even-Lavie nozzle, previous work from our lab demonstrated 5 K rotational temperatures for isoquinoline under similar conditions.[35] Therefore, we expect that complexes formed under these conditions will have constituent moieties at the ground vibrational levels: $^3[^1\mathrm{M}(v = 0) - {}^3\mathrm{O}_2\ (v = 0)]$. The complex may then undergo a transition to an excited state giving $^1O_2$ in the ground vibrational level and the triplet organic moiety as shown in eq 4:

$$^3[^1\mathrm{M}(v = 0) - {}^3\mathrm{O}_2(v = 0)] + h\nu \rightarrow {}^3[^3\mathrm{M}(v) - {}^1\mathrm{O}_2(v = 0)] \tag{4}$$

During this excitation, the triplet organic moiety may be formed vibrationally excited, $^3\mathrm{M}(v)$, which is then followed by complex dissociation. We can estimate the transition energy for eq 4 as the sum of the singlet to triplet vibrational excitation of the organic moiety, $E[^3\mathrm{M}(v) \leftarrow {}^1\mathrm{M}(v = 0)]$, the $^1O_2$ term energy, $E[^1\mathrm{O}_2(v = 0) \leftarrow {}^3\mathrm{O}_2(v = 0)]$ and the difference between the ground and excited state complex dissociation energies:

$$E_{\mathrm{exc}} = E[^3\mathrm{M}(v) \leftarrow {}^1\mathrm{M}(v = 0)] + E[^1\mathrm{O}_2(v = 0) \leftarrow {}^3\mathrm{O}_2(v = 0)] + (D_0'' - D_0') \tag{5}$$

and we schematically illustrate eq 5 in Figure S12 of the Supporting Information.

Using eq 5 requires the singlet to triplet excitation energy for the organic moiety, which has been reported for acridine.[46] The reported acridine spectrum shows a series of bands spaced by 1400 cm^{-1} with a full width at half-maximum (fwhm) of about 700 cm^{-1} and our electronic structure calculations identified several vibrational modes of triplet acridine near 1400 cm^{-1} all having substantial in-plane C−H wagging character. From the singlet to triplet absorption spectrum, the $v' = 3 \leftarrow v'' = 0$ acridine band was located at 20040 cm^{-1}.[46] In eq 5, the ground and excited state binding energies must be non-negative and the difference between these should be much smaller than the acridine-O_2 ground state binding energy, which Table 1 gives as 514 or 480 cm^{-1} from the PBE/aug-cc-pVQZ//D3 or M06/aug-cc-pVQZ//D3 calculations, respectively. Neglecting the third term in eq 5 and using the $^1O_2$ term energy of 7900 cm^{-1} (0.98 eV), we calculate a transition to the vibrationally excited $^3[^3\mathrm{Ac}(v = 3) - {}^1\mathrm{O}_2\ (v = 0)]$ complex to be about 27940 cm^{-1}. This excitation energy is close to the energy of our 355 nm photon, 28170 cm^{-1}, particularly given the 700 cm^{-1} fwhm bands from the acridine spectrum.[46] Thus, we expect the 355 nm transition for acridine-O_2 may form a complex having triplet acridine in the $\nu = 3$ vibrational level with about 4200 cm^{-1} of vibrational energy.

Previous work has shown a complex with a vibrationally excited moiety may undergo vibrational predissociation to form translationally cold products, and this phenomenon has been explained using energy gap or momentum gap arguments.[47] Following momentum gap arguments, the vibrational predissociation lifetime, τ, is related to the total change in the translational, rotational, and vibrational quantum numbers, Δn_{total}, as $1/\tau = (10^{13}\text{s})\exp(-\pi\Delta n_{\text{total}})$.[48] Qualitatively, for a complex with a vibrationally excited moiety, the energy transfer between combinations of vibrational modes results in small changes to the total quantum number giving short excited state lifetimes. Alternatively, vibrational to translational energy transfer leads to large total changes in quantum numbers, since the latter are low energy states. Thus, transferring vibrational energy into translational energy is inefficient and vibrational predissociation can result in translationally slow products, which is consistent with our observations for the acridine-O_2 system. Moreover, as the 1400 cm^{-1} C−H wagging modes of acridine have predominantly in-plane vibrational character, we expect these modes to be weakly coupled to the dissociation coordinate for a complex with O_2 above the plane of the ring system.

For phenalenone, Table 2 shows a 0.73 eV difference between the vertical and adiabatic triplet energies, and for β-ionone, our previous calculations gave the vertical triplet energy to be 3.30 eV with an adiabatic energy of 2.04 eV.[14] These large differences between vertical and adiabatic triplet energy suggest that excitation from the ground state of either M-O_2 complex may result in a vibrationally excited organic moiety. Moreover, for phenalenone and β-ionone, the available energy was between 0.52 and 0.54 eV or between 0.53 and 0.87 eV, respectively, and for both systems, the experimental $P(E_T)$ is biased to lower CM translational energy relative to the statistical prediction. This observation is also consistent with vibrational predissociation giving translationally slow products. Finally, at much lower available energies, as for quinoline, pyridine, and fluorenone, less energy is available for significant vibrational excitation of the organic moiety, which may then result in the apparent statistical $P(E_T)$.

We also point out that for all complexes, the $^1O_2$ rotational temperature is below about 80 K, which indicates inefficient energy disposal into rotation. This is also consistent with expectations from vibrational predissociation since disposal of vibrational energy into rotation results in large total quantum number changes, which is disfavored. Moreover, the low rotational temperature may also indicate the excited state potential energy surface for these systems has a weak angular anisotropy, resulting in very little torque on the O_2 fragment.

We can also consider energy partitioning from ultraviolet photodissociation for isoprene-O_2. For isoprene-O_2, Vidma et al. used resonant ionization at 226 nm to observe fast O ($^3P_0$) atoms with kinetic energies of 0.74 ± 0.05 eV.[8] The 226 nm photolysis of $^1O_2$ ($\nu = 0$) results in O (^3P) atoms with a kinetic energy of 0.64 eV and so the observed fast O atoms were assigned to the formation of $^1O_2$ through a DSF mechanism. Baklanov et al. used the same detection scheme to observe $^1O_2$ from a variety of M-O_2 complexes and concluded that most $^1O_2$ should be produced in the ground vibrational level based on Franck−Condon factors, which was consistent with experimental observations.[49] Baklanov et al. also concluded the maximum energy for the DSF absorption band to be the sum of the organic vertical triplet energy and the $^1O_2$ term energy, with the former taken as 3.2 eV for isoprene formed in the lowest triplet state. Later work from Bogomolov et al. used a novel (1 + 1′) + 1 REMPI scheme to detect $^1O_2$ from isoprene-O_2 using a single dye laser to provide both UV and visible photons.[50] The resulting REMPI spectra displayed features that were assigned to resonant ionization of $^1O_2$ (a $^1\Delta_g$) or $^3O_2$ (X $^3\Sigma_g^-$) and VMI data was reported. From the O_2^+ VMI data, the kinetic energy distribution was reported at three photon energies: 5.428, 5.434, and 5.497 eV, and using the reported 3.2 eV *vertical* triplet state energy, the available energy is greater than 1.2 eV. At 5.428 eV photon energy, the O_2^+ ion image showed only a molecular beam spot with a narrow kinetic energy distribution. At 5.434 eV photon energy, the kinetic energy distribution extended to ∼0.3 eV and was fit to a 280 K Boltzmann distribution, while increasing the photon energy to 5.497 eV resulted in a kinetic energy distribution that extended to about 0.6 eV and was fit to a 940 K Boltzmann distribution.

Thus, the kinetic energy distribution from isoprene-O_2 photodissociation at both 5.434 and 5.497 eV resulted in relatively slow $^1O_2$ with the highest observed kinetic energies well below the available energy. Moreover, from the REMPI spectra, the $^1O_2$ product is produced in the lowest vibrational levels. These results collectively indicate that a substantial fraction of energy is partitioned into the isoprene moiety during photodissociation, which is consistent with our current experiments with aza-aromatic and aromatic carbonyl-containing complexes.

Finally, we again note that the statistical kinetic energy distributions presented in this work were generated assuming the formation of the triplet organic moiety. Since the REMPI spectra clearly demonstrate $^1O_2$, the overall similarity between the experimental and statistical $P(E_T)$ is consistent with the excitation: $^3(^1M - {}^3O_2) + h\nu \rightarrow {}^3(^3M^* - {}^1O_2)$. At low available energies, the statistical distribution nearly reproduces the experimental observations, but at high available energies, above ∼0.2 eV, the statistical distribution overpredicts the experiment. We also note that if the organic moiety was formed in the ground electronic state, then the maximum available energy would be larger by the adiabatic triplet energies given in Table 2. In this case, the disagreement between the experimental distribution and the statistical prediction would further increase due to the much larger available energy.

V. CONCLUSIONS

In this study, we have reported a modified synthesis of 1*H*-phenalen-1-one, which facilitates reaction workup and subsequent chromatographic purification. We have also assessed several DFT-based electronic structure methods to evaluate the cluster binding energy and conclude that the PBE and M06 methods provide satisfactory results. Compared with our previous MP2 calculations, these DFT methods may be more easily extended to larger organic molecules, and we have used these methods to also determine the adiabatic and vertical triplet energies for the organic molecules studied here. Our experimental REMPI spectra demonstrate that $^1O_2$ is formed during the excitation and we have shown that with proper chromophore choice, we can form both the triplet organic moiety and $^1O_2$ following excitation at 355 nm. By comparing the experimental CM kinetic energy distribution with a Prior distribution, we conclude that as the available energy increases, the products are formed with less CM translational energy relative to the statistical prediction. We argue that during the excitation of acridine-O_2, the organic moiety may be vibrationally excited and the cold $P(E_T)$ is due to vibrational predissociation of the complex. Finally, a similar dissociation mechanism may account for the observed $P(E_T)$ for the phenalenone-O_2 and β-ionone-O_2 complexes.

■ ASSOCIATED CONTENT

Supporting Information

The Supporting Information is available free of charge at https://pubs.acs.org/doi/10.1021/acs.jpca.4c00143.

> Infrared spectrum of 1*H*-phenalen-1-one; ^{1}H and ^{13}C NMR spectra of 1*H*-phenalen-1-one; mass spectrum of 1*H*-phenalen-1-one; figures showing structure of M-O_2 complexes (M = pyridine, phenalenone, fluorenone, acridine); tables giving Cartesian coordinates for M-O_2 complexes (M = pyridine, phenalenone, fluorenone, acridine) optimized at PBE/aug-cc-pVQZ level; tables giving vibrational frequencies for the lowest singlet and triplet states of pyridine, phenalenone, fluorenone, and acridine at the at PBE/aug-cc-pVQZ level; tables giving the calculated vertical and adiabatic triplet energies for phenalenone, fluorenone, pyridine, and acridine; $^1O_2$ REMPI spectra from photodissociation of M-O_2 (M = fluorenone, pyridine, acridine); and figure illustrating the relationships described by eq (5) from text (PDF)

■ AUTHOR INFORMATION

Corresponding Author

Bradley F. Parsons − *Department of Chemistry and Biochemistry 2500 California Plaza, Creighton University, Omaha, Nebraska 68178, United States*; orcid.org/0000-0002-0749-8257; Phone: 402-280-3735; Email: bparsons@creighton.edu

Authors

Martin R. Hulce − *Department of Chemistry and Biochemistry 2500 California Plaza, Creighton University, Omaha, Nebraska 68178, United States*; orcid.org/0000-0001-8849-8082

John R. Ackerman − *Department of Chemistry and Biochemistry 2500 California Plaza, Creighton University, Omaha, Nebraska 68178, United States*; orcid.org/0009-0007-4161-1675

Kylie A. Reardon − *Department of Chemistry and Biochemistry 2500 California Plaza, Creighton University, Omaha, Nebraska 68178, United States*

Emerson S. Pappas − *Department of Chemistry and Biochemistry 2500 California Plaza, Creighton University, Omaha, Nebraska 68178, United States*

Lauren E. Kettler − *Department of Chemistry and Biochemistry 2500 California Plaza, Creighton University, Omaha, Nebraska 68178, United States*

Complete contact information is available at: https://pubs.acs.org/10.1021/acs.jpca.4c00143

Notes

The authors declare no competing financial interest.

■ ACKNOWLEDGMENTS

This work was supported by the National Science Foundation under grant number CHE-2150871.

■ REFERENCES

(1) Huber, K. P.; Herzberg, G. H. Constants of Diatomic Molecules. In *NIST Chemistry WebBook*; Linstrom, P. J.; Mallard, W. G., Eds.; NIST Standard Reference Database Number 69, National Institute of Standards and Technology: Gaithersburg MD, (retrieved Dec 20, 2023). http://webbook.nist.gov.

(2) Kanofsky, J. R. Photosensitization. *Singlet Oxygen Vol. 1.*; Royal Society of Chemistry: Cambridge, U.K., 2016.

(3) Parker, D. H. Laser Photochemistry of Molecular Oxygen. *Acc. Chem. Res.* **2000**, *33*, 563−571.

(4) DeBoer, G.; Young, M. A. Photochemistry and Dynamics of C_6H_6-O_2 Clusters at 226 nm. *J. Chem. Phys.* **1997**, *106*, 5468−5477.

(5) DeBoer, G.; Prince, A. P.; Young, M. A. Charge-transfer Mediated Photochemistry in Alkene-O_2 Complexes. *J. Chem. Phys.* **2001**, *115*, 3112−3120.

(6) Guidoni, G. A.; Paladini, A.; Veneziani, M.; Naaman, R.; Di Palma, T. M. Laser Excited Charge Transfer Processes in Oxygen Organic Molecules Mixtures: O (^3P_j) Formation. *Appl. Surf. Sci.* **2000**, *154−155*, 186−191.

(7) Parsons, B. F.; Chandler, D. W. On the Dissociation of van der Waals Clusters of X_2−Cyclohexane (X = O, Cl) Following Charge-Transfer Excitation in the Ultraviolet. *J. Phys. Chem. A* **2003**, *107*, 10544−10553.

(8) Vidma, K. V.; Frederix, P. W. J. M.; Parker, D. H.; Baklanov, A. V. Photodissociation of van der Waals Clusters of Isoprene with Oxygen, C_5H_8-O_2 in the Wavelength Range 213−277 nm. *J. Chem. Phys.* **2012**, *137*, No. 054305.

(9) Baklanov, A. V.; Parker, D. H. Weakly Bound Environment of Molecular Oxygen as a Catalyst of Photooxidation. *Kinet. Catal.* **2020**, *61*, 174−197.

(10) Kasama, K.; Kikuchi, K.; Yamamoto, S.; Ujiie, K.; Nishida, Y.; Kokubun, H. Relaxation Mechanism of Excited Acridine in Non-reactive Solvents. *J. Phys. Chem.* **1981**, *85*, 1291−1296.

(11) Ghoshal, S. K.; Maiti, A. K.; Kastha, G. S. Luminescence Properties of Ultrapure Pyridine. *J. Lumin.* **1984**, *31−32*, 541−545.

(12) Soep, B.; Mestdagh, J.-M.; Briant, M.; Gaveau, M.-A.; Poisson, L. Direct Observation of Slow Intersystem Crossing in an Aromatic Ketone, Fluorenone. *Phys. Chem. Chem. Phys.* **2016**, *18*, 22914−22920.

(13) Flors, C.; Nonell, S. On the Phosphorescence of 1*H*-Phenalen-1-one. *Helv. Chim. Acta* **2001**, *84*, 2533−2539.

(14) Parsons, B. F.; Freitag, M. A.; Warder, H. J. Singlet O_2 Produced by Ultraviolet Excitation of the β-ionone-O_2 Complex. *J. Phys. Chem. A* **2021**, *125*, 8649−8657.

(15) Parsons, B. F.; Rivera, M. R.; Freitag, M. A.; Reardon, K. A.; Pappas, E. S.; Rausch, J. T. Singlet O_2 from Ultraviolet Excitation of the Quinoline-O_2 Complex. *J. Phys. Chem. A* **2023**, *127*, 4957−4963.

(16) Neese, F. The ORCA Program System. *WIREs Comput. Mol. Sci.* **2012**, *2*, 73−78.

(17) Perdew, J. P.; Burke, K.; Ernzerhof, M. Generalized Gradient Approximation Made Simple. *Phys. Rev. Lett.* **1996**, *77*, 3865−3868.

(18) Lee, C.; Yang, W.; Parr, R. G. Development of the Colle-Salvetti Correlation-energy Formula into a Functional of the Electron Density. *Phys. Rev. B* **1988**, *37*, 785−789.

(19) Becke, A. D. Density-functional Exchange-energy Approximation with Correct Asymptotic Behavior. *Phys. Rev. A* **1988**, *38*, 3098−3100.

(20) Stephens, P. J.; Devlin, F. J.; Chabalowski, C. F.; Frisch, M. J. Ab Initio Calculation of Vibrational Absorption and Circular Dichroism Spectra Using Density Functional Force Fields. *J. Phys. Chem.* **1994**, *98*, 11623−11627.

(21) Zhao, Y.; Truhlar, D. G. The M06 Suite of Density Functionals for Main Group Thermochemistry, Thermochemical Kinetics, Noncovalent Interactions, Excited States, and Transition Elements:

Two New Functionals and Systematic Testing of Four M06-class Functionals and 12 Other Functionals. *Theor. Chem. Acc.* **2008**, *120*, 215−241.

(22) Kendall, R. A.; Dunning, T. H.; Harrison, R. J. Electron Affinities of the First-row Atoms Revisited. Systematic Basis Sets and Wave Functions. *J. Chem. Phys.* **1992**, *96*, 6796−6806.

(23) Grimme, S.; Ehrlich, S.; Goerigk, L. Effect of the Damping Function in Dispersion Corrected Density Functional Theory. *J. Comput. Chem.* **2011**, *32*, 1456−1465.

(24) Boys, S. F.; Bernardi, F. The Calculation of Small Molecular Interactions by the Differences of Separate Total Energies. Some Procedures with Reduced Errors. *Mol. Phys.* **1970**, *19*, 553−566.

(25) Jing, Y.; Xu, Q.; Chen, M.; Shao, X. Pyridone-containing Phenalenone-based Photosensitizer Working Both Under Light and in the Dark for Photodynamic Therapy. *Bioorg. Med. Chem.* **2019**, *27*, 2201−2208.

(26) Pal, M.; Bearne, S. L. Synthesis of Coenzyme A Thioesters Using Methyl Acyl Phosphates in an Aqueous Medium. *Org. Biomol. Chem.* **2014**, *12*, 9760−9763.

(27) Koelsch, C. F.; Anthes, J. A. Studies in the Perinaphthene Series. IV. Some Attempts to Synthesize 9-phenyl-7-perinaphthanone. *J. Org. Chem.* **1941**, *6*, 558−565.

(28) Even, U. The Even-Lavie Valve as a Source for High Intensity Supersonic Beam. *EPJ Technol. Instrum.* **2015**, *2*, 1−22, DOI: 10.1140/epjti/s40485-015-0027-5.

(29) Even, U.; Jortner, J.; Noy, D.; Lavie, N.; Cossart-Magos, C. Cooling of Large Molecules Below 1 K and He Clusters Formation. *J. Chem. Phys.* **2000**, *112*, 8068−8071.

(30) Eppink, A. T. J. B.; Parker, D. H. Velocity Map Imaging of Ions and Electrons Using Electrostatic Lenses: Application in Photoelectron and Photofragment Ion Imaging of Molecular Oxygen. *Rev. Sci. Instrum.* **1997**, *68*, 3477−3484.

(31) Johnson, R. D.; Long, G. R.; Hudgens, J. W. Two Photon Resonance Enhanced Multiphoton Ionization Spectroscopy of Gas Phase O_2 a $^1\Delta_g$ Between 305−350 nm. *J. Chem. Phys.* **1987**, *87*, 1977−1981.

(32) Morrill, J. S.; Ginter, M. L.; Hwang, E. S.; Slanger, T. G.; Copeland, R. A.; Lewis, B. R.; Gibson, S. T. Two-photon REMPI Spectra from a $^1\Delta_g$ and b $^1\sum_g^+$ to d $^1\Pi_g$ in O_2. *J. Mol. Spectrosc.* **2003**, *219*, 200−216.

(33) Eppink, A. T. J. B.; Parker, D. H. Methyl Iodide A-band Decomposition Study by Photofragment Velocity Imaging. *J. Chem. Phys.* **1998**, *109*, 4758−4767.

(34) Parsons, B. F.; Szpunar, D. E. Investigation of O_2-X (X = Pyrrole or Pyridine) Cluster Photodissociation Near 226 nm. *J. Phys. Chem. A* **2020**, *124*, 10152−10161.

(35) Krogmeier, T. J.; Pappas, E. S.; Reardon, K. A.; Rivera, M. R.; Head-Marsden, K.; Parsons, B. F.; Schlimgen, A. W. Characterizing the Origin Band Spectrum of Isoquinoline with Resonance Enhanced Multiphoton Ionization and Electronic Structure Calculations. *J. Chem. Phys.* **2023**, *159*, No. 134305.

(36) Western, C. M. PGOPHER: A Program for Simulating Rotational, Vibrational and Electronic Spectra. *J. Quant. Spectrosc. Radiat. Transfer* **2017**, *186*, 221−242.

(37) Dribinski, V.; Ossadtchi, A.; Mandelshtam, V. A.; Reisler, H. Reconstruction of Abel-Transformable Images: The Gaussian Basis-set Expansion Abel Transform Method. *Rev. Sci. Instrum.* **2002**, *73*, 2634−2642.

(38) Hiraya, A.; Achiba, Y.; Kimura, K.; Lim, E. C. Identification of the Lowest Energy nπ* States in Gas-phase Polycyclic Monoazines: Quinoline and Isoquinoline. *J. Chem. Phys.* **1984**, *81*, 3345−3347.

(39) Muzny, C. Thermodynamics Source Database. In *NIST Chemistry WebBook*; Linstrom, P. J.; Mallard, W. G., Eds.; NIST Standard Reference Database Number 69, National Institute of Standards and Technology: Gaithersburg MD, (retrieved Dec 20 2023). http://webbook.nist.gov.

(40) Domalski, E. S.; Hearing, E. D. Condensed Phase Heat Capacity Data. In *NIST Chemistry WebBook*; Linstrom, P. J.; Mallard, W. G., Eds.; NIST Standard Reference Database Number 69, National Institute of Standards and Technology: Gaithersburg MD, (retrieved Dec 20, 2023). http://webbook.nist.gov.

(41) Urbain, P.; Leyh, B.; Remacle, F.; Lorquet, A. J.; Flammang, R.; Lorquet, J. C. Unimolecular Reaction Dynamics from Kinetic Energy Release Distributions. III. A Comparative Study of the Halogenobenzene Cations. *J. Chem. Phys.* **1999**, *110*, 2911−2921.

(42) Anton, M. F.; Moomaw, W. R. Luminescence and Hydrogen Bonding in Quinoline and Isoquinoline. *J. Chem. Phys.* **1977**, *66*, 1808−1818.

(43) Chattopadhyay, S. K.; Kumar, C. V.; Das, P. K. Triplet Excitation Transfer Involving β-ionone. A Kinetic Study by Laser Flash Photolysis. *Photochem. Photobiol.* **1985**, *42*, 17−24.

(44) Cerfontain, H.; Geenevasen, J. A. J.; van Noort, P. C. M. Photochemistry of Dienones. Part VII. On the Photosensitized Isomerization of (E)-β-ionone and Its Isomeric α-pyran. Evidence for Exciplex Formation Between the α-pyran and Fluoren-9-one. *J. Chem. Soc., Perkin Trans. 2.* **1980**, 1057−1062.

(45) Montalti, M.; Credi, A.; Prodi, L.; Gandolfi, M. T. *Handbook of Photochemistry*; CRC Press: Boca Raton, FL, 2006.

(46) Evans, D. F. Perturbation of Singlet-triplet Transitions of Aromatic Molecules by Oxygen Under Pressure. *J. Chem. Soc.* **1957**, *0*, 1351−1357.

(47) Lester, M. I. Vibrational Predissociation Dynamics of van der Waals Complexes: Product Rotational State Distributions. *Adv. Chem. Phys.* **1996**, *96*, 51−102.

(48) Ewing, G. E. Selection Rules for Vibrational Energy Transfer: Vibrational Predissociation of van der Waals Molecules. *J. Phys. Chem.* **1987**, *91*, 4662−4671.

(49) Baklanov, A. V.; Bogomolov, A. S.; Pyryaeva, A. P.; Bogdanchikov, G. A.; Kochubei, S. A.; Farooq, Z.; Parker, D. H. Singlet Oxygen Photogeneration from X-O_2 van der Waals Complexes: Double Spin-flip vs. Charge-transfer Mechanism. *Phys. Chem. Chem. Phys.* **2015**, *17*, 28565−28573.

(50) Bogomolov, A. S.; Dozmorov, N. V.; Kochubei, S. A.; Baklanov, A. V. REMPI Detection of Singlet Oxygen $^1O_2$ Arising from the UV-photodissociation of van der Waals Complex Isoprene-oxygen C_5H_8-O_2. *Chem. Phys. Lett.* **2018**, *692*, 271−276.